Energy & Environmental Science

ROYAL SOCIETY OF CHEMISTRY

PAPER

View Article Online
View Journal | View Issue

Check for updates

Cite this: *Energy Environ. Sci.*, 2024, **17**, 5260

Activating lattice oxygen by a defect-engineered Fe_2O_3–CeO_2 nano-heterojunction for efficient electrochemical water oxidation†

Qiuping Huang,‡[a] Guang-Jie Xia,‡[b] Bo Huang,[a] Dongling Xie,[a] Jianan Wang,[a] Dan Wen,[a] Dunmin Lin,[a] Chenggang Xu,[a] Lei Gao,[c] Zhenduo Wu,[d] Jinqi Wu,[e] Fengyu Xie,*[a] Wenhan Guo*[b] and Ruqiang Zou*[c]

Received 11th April 2024,
Accepted 7th June 2024

DOI: 10.1039/d4ee01588f

rsc.li/ees

The sluggish anodic oxygen evolution reaction (OER) is currently the major hinderance for hydrogen production from water splitting. Iron-based materials are promising cost-effective candidates for OER electrocatalysts, however their low intrinsic activity limits their performance. Here we report a defect-engineered Fe_2O_3–CeO_2 heterojunction with rich oxygen vacancies (Fe_2O_3@CeO_2–O_V), exhibiting ultra-low overpotential of 172 mV at 10 mA cm^{-2} and 317 mV at 1000 mA cm^{-2}, respectively, alongside superior stability and durability. Advanced characterization and density functional theory calculations demonstrate that defect engineering combined with heterojunction formation activates the lattice oxygen, switching the reaction pathway from the conventional adsorbate evolution mechanism (AEM) to the lattice oxygen mechanism (LOM). The oxygen vacancies are revealed to form preferably on CeO_2 and induce not only electronic but also geometric modulation, contributing to strong Fe_2O_3–CeO_2 interfacial interaction and charge transfer from CeO_2 to Fe_2O_3, facilitating the O_2 desorption and boosting the intrinsic activity.

Open Access Article. Published on 14 kesäkuuta 2024. Downloaded on 13.5.2026 1.36.10.
This article is licensed under a Creative Commons Attribution-NonCommercial 3.0 Unported Licence.

Broader context

Water splitting powered by renewable power sources (like solar, wind or tide energy) is the most promising approach to produce green hydrogen for large-scale commercialization applications. The sluggish anodic oxygen evolution reaction (OER) is regarded as a major challenge for current overall water electrolysis research. Activating the lattice oxygen of oxide-based catalysts presents a fascinating new approach to switch the reaction pathway from a traditional adsorbate evolution mechanism (AEM) to the novel lattice oxygen mechanism (LOM), by passing the linear scaling limitations and thus reducing the overpotentials and thereby total energy consumption. In this work, we report a combination of defect engineering and heterojunction interfacial engineering to successfully construct a defect-rich Fe_2O_3–CeO_2 nano-heterojunction material (denoted as Fe_2O_3@CeO_2-O_V) loaded onto porous nickel foam (NF) as self-supporting electrode for efficient OER catalysis. Our approach successfully activates the lattice oxygen, and this heterojunction electrode with rich oxygen vacancies exhibits excellent OER catalytic performance with a low potential of 172 mV at 10 mA cm^{-2} and 317 mV at 1000 mA cm^{-2}, among the highest data for reported Fe-based catalysts, together with superior stability and durability. This work may provide new methodological and theoretical inspirations for researchers from broader research contexts.

Introduction

Hydrogen as one of the cleanest energy carriers is essential for establishing a carbon-free sustainable eco-energy system.[1,2] Electrocatalytic overall water splitting (OWS) combined with renewable power sources is a promising approach for mass production of green hydrogen from earth-abundant and pollutant-free water.[3–6] The anodic oxygen evolution reaction (OER) is currently believed to be the major bottleneck of water electrolysis due to the sluggish reaction kinetics and limited performance of electrocatalysts.[7,8] Catalysts following the traditional adsorbate evolution mechanism (AEM) could not

[a] *College of Chemistry and Materials Science, Sichuan Normal University, Chengdu 610066, P. R. China. E-mail: xiefengyu@sicnu.edu.cn*
[b] *Dongguan Key Laboratory of Interdisciplinary Science for Advanced Materials and Large-Scale Scientific Facilities, School of Physical Sciences, Great Bay University, Dongguan 523000, China. E-mail: whguo@gbu.edu.cn*
[c] *School of Materials Science and Engineering, Peking University, Beijing 100871, China. E-mail: rzou@pku.edu.cn*
[d] *City University of Hong Kong (Dongguan), Dongguan 523000, China*
[e] *Shimadzu China Co. Ltd, Guangzhou, 510656, China*

† Electronic supplementary information (ESI) available. See DOI: https://doi.org/10.1039/d4ee01588f

‡ Qiuping Huang and Guang-Jie Xia contributed equally to this work.

This journal is © The Royal Society of Chemistry 2024

Open Access Article. Published on 14 kesäkuuta 2024. Downloaded on 13.5.2026 1.36.10.
This article is licensed under a Creative Commons Attribution-NonCommercial 3.0 Unported Licence.

overcome the intrinsic overpotential threshold of around 370 mV limited by the Sabatier's principle and linear-scaling relationship of key intermediates (*O, *OH, *OOH, *etc.*), impeding the improvement of catalytic performance.[9,10] Recent studies have however revealed the critical role of lattice oxygen involved in the water oxidation process *via* formation and healing of surficial oxygen vacancies (O_V) in certain oxide and (oxy)hydroxide materials, known now as the lattice oxygen mechanism (LOM).[11] The LOM-based OER proceeds through decoupled proton and electron transfer, bypassing the limitation of the linear scaling AEM, thus reducing overpotential and thereby energy consumption. Therefore, developing novel OER electrocatalysts based on the LOM has become one of the research frontiers of water splitting.

Yang Shao-Horn's group reported the early experimental verification of lattice oxygen participation in the OER for (La, Sr) $CoO_{3-\delta}$ perovskite oxides by combining on-line electrochemical mass spectrometry (OLEMS) ^{18}O-isotopic-labeled measurements and density functional theory (DFT) calculations,[12] followed by numerous reports on other materials including perovskites,[13] spinels,[14] bimetallic oxyhydroxides[15] and layered double hydroxides (LDHs).[16] In addition to the above-mentioned materials, transition-metal oxides (TMOs) have been extensively studied as potential LOM-OER catalysts owing to their high stability, low cost and easy synthesis. Experimental and theoretical studies have shown that increasing the covalency of metal–oxygen bonds is key to triggering lattice-oxygen oxidation of TMOs.[17] However, activation of lattice oxygen could conversely deteriorate the durability of materials due to the formation of coordination-unsaturated metal sites during the reaction, leading to metal leaching and thus collapse or phase transition of the base material.[18] Consequently, achieving both high activity and stability, especially under industrially meaningful high current densities, remains a great challenge for most of the LOM-based OER electrocatalysts.

Iron (Fe) is the most abundant and inexpensive metal element widely applied, and Fe-based materials are promising candidates for large-scale water splitting, despite their unsatisfactory low catalytic performance.[19] The presence of Fe could induce the downshift of the metal d-band to penetrate through the 2p band of oxygen ligands and increase the covalency of M–O, leading to trigger-on of the LOM route for the OER, as well as inhibit the dissolution of metal species.[20] Unfortunately, Fe-based metal oxides following the LOM for efficient water splitting are rarely reported, mostly due to the low intrinsic activity of Fe-oxides.[21] Constructing heterojunction nanostructures is a feasible way to modulate both the electronic structure and metal–O bonding properties of oxide materials. The different working functions and band structures of the two sides of the heterojunction would induce interfacial charge transfer and redistribution, contributing to the intriguing physiochemical properties,[22] like the shifting of the d-band center,[23] modulation of surficial electron density[24] and largely increased concentration of local disorders and defects.[25] Our group has recently reported the self-assembled bimetallic NiFe-MOF-74@NiFe-LDH nano-heterojunction self-supporting electrode as an electrocatalyst for efficient alkaline OER. DFT calculations revealed that the OER reaction took place at the interfacial oxygen defect sites, and the catalyst presented excellent OER performance aligning with the LOM pathway.[26] These results demonstrate the promising potential of heterojunction materials in the LOM-based OER. In parallel to the above tactics, defect engineering is another promising strategy to modulate the intrinsic reactivity of surficial metal sites for TMOs. Defects play an essential role in the LOM-mediated OER, and the rich O_V sites introduced by defect engineering could change the coordination environment of metal centers, so as to modulate both the M–O bonding strength and charge distribution, exposing more active sites and promoting charge transfer, ultimately enhancing the reactivity of lattice oxygens. Inspired by the aforementioned design rationales, defect engineering across heterojunction interfaces provides an intriguing approach to transform the OER mechanism of Fe-based metal oxides from the AEM to the LOM, breaking the linear limitation of the traditional AEM pathway and enhancing the intrinsic activity.

Herein, we report a defect-rich Fe_2O_3/CeO_2 nano-heterojunction material (denoted as $Fe_2O_3@CeO_2–O_V$) loaded onto porous nickel foam (NF) as a self-supporting electrode for efficient OER catalysis. A two-step solvothermal reaction was applied to synthesize the heterojunction material, followed by an additional calcination process to create abundant oxygen vacancies on the catalyst surface. Diffractional and microscopic analyses revealed that the hierarchical hydrangea-like microstructures consisted of Fe_2O_3 nanoflowers covered with CeO_2 nanoparticles, while X-ray photoelectron spectroscopy (XPS), X-ray absorption fine structure (XAFS) and electron paramagnetic resonance (EPR) confirmed the formation of additional oxygen vacancies. The combination of XPS, ^{18}O-isotopic labelling mass spectroscopy and density functional theory (DFT) calculations validated the participation of lattice oxygen induced by the defect-rich initial structure, enabling the switching from the AEM to the LOM. Specifically, the oxygen vacancies significantly strengthened the interaction between Fe_2O_3 substrates and above CeO_2 nanoparticles, enhancing their charge transfer at the heterojunction interface, facilitating the O_2 desorption, thus promoting the intrinsic OER activity. The resultant defect-rich $Fe_2O_3@CeO_2–O_V$ exhibited superior OER performance with a low overpotential of 172 mV at 10 mA cm^{-2}, among the highest data reported for Fe-based catalysts. More intriguingly, $Fe_2O_3@CeO_2–O_V$ could deliver a large current density of 1000 mA cm^{-2} at an ultralow overpotential of 317 mV. Excellent activity and stability were also verified in a membrane-based flow cell to simulate practical industrial scenarios, confirming the great potential of $Fe_2O_3@CeO_2–O_V$ for commercial applications.

Results and discussion

The synthetic process of the self-supporting $Fe_2O_3@CeO_2–O_V$ nano-heterojunction electrode on NF is illustrated in Fig. 1a

Open Access Article. Published on 14 kesäkuuta 2024. Downloaded on 13.5.2026 1.36.10.
This article is licensed under a Creative Commons Attribution-NonCommercial 3.0 Unported Licence.

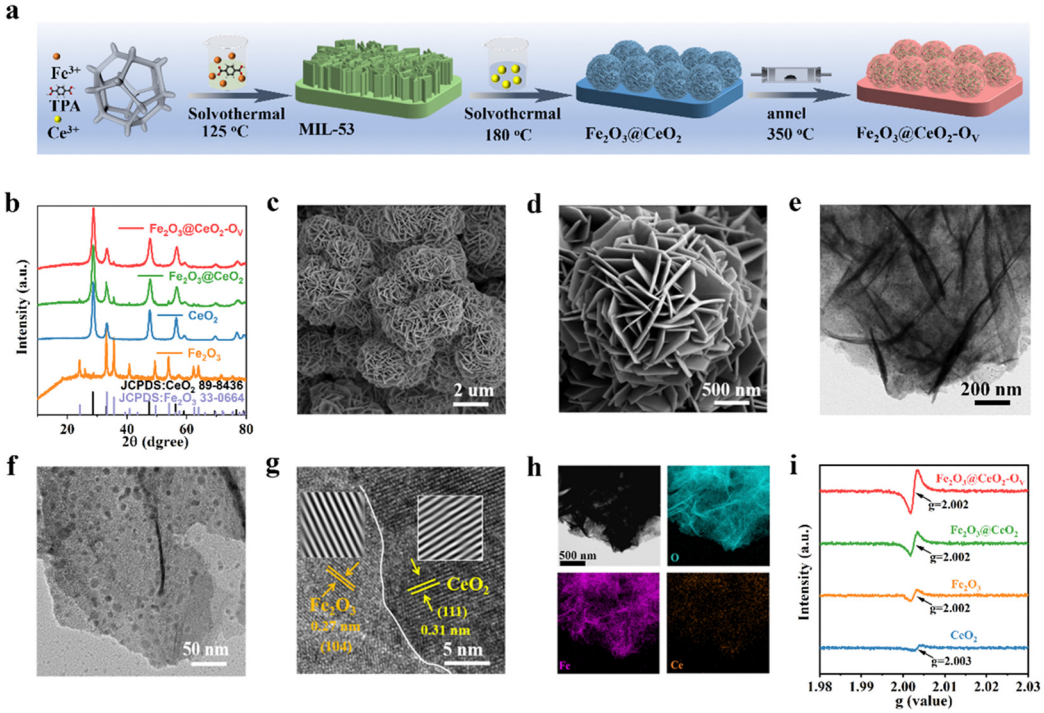

Fig. 1 Characterization of Fe_2O_3@CeO_2–O_V. (a) Schematic illustration of the synthetic process for Fe_2O_3@CeO_2–O_V. (b) XRD patterns of Fe_2O_3@CeO_2–O_V, Fe_2O_3@CeO_2, Fe_2O_3 and CeO_2. (c) and (d) SEM images of Fe_2O_3@CeO_2–O_V. (e) and (f) TEM images of Fe_2O_3@CeO_2–O_V. (g) HRTEM image of Fe_2O_3@CeO_2–O_V. (h) EDX elemental mapping of Fe_2O_3@CeO_2–O_V. (i) EPR signals for Fe_2O_3@CeO_2–O_V, Fe_2O_3@CeO_2, Fe_2O_3 and CeO_2.

and detailed experimental protocols are given in the ESI.† Initially, self-supported Fe-based metal–organic framework (MOF) MIL-53 nanosheet arrays were grown onto pre-cleansed NF sheets *via* solvothermal reactions in the mixed solution of Fe^{3+} and terephthalic acid (TPA) in *N*,*N*-dimethylformamide (DMF). Successful formation of MIL-53 on the NF surface was confirmed by powder X-ray diffraction (PXRD), Fourier transform infrared spectroscopy (FT-IR) and Raman spectroscopy, in accordance with previous reports[27] (Fig. S1, ESI†). The MOF precursors were subjected to a secondary hydrothermal treatment in Ce^{3+}-containing solution to obtain Fe_2O_3@CeO_2 nanoheterojunction electrodes with nanoflower-like morphology, which were further annealed in an argon atmosphere to acquire defect-engineered Fe_2O_3@CeO_2–O_V electrodes. For comparison, two comparative samples, named Fe_2O_3 (synthesized directly from Fe^{3+} instead of MOF precursors) and CeO_2 (without the addition of Fe^{3+} species) were also synthesized. PXRD patterns were collected for all samples to determine the phase information (Fig. 1b). After the secondary hydrothermal treatment, the peaks of MIL-53 disappeared, replaced by the peaks of Fe_2O_3 (JCPDS: 33-0644) and CeO_2 (JCPDS: 34-0394), indicating the complete transformation of MOF precursors to oxide materials. The weak diffraction intensities of Fe_2O_3 peaks might be due to the low crystallinity and amorphization during hydrolysis of MOF precursors, while the signals from Fe_2O_3 further weakened after annealing, due to the introduction of additional oxygen vacancies and deterioration of local coordination structures. Rietveld refinement further verified that Fe_2O_3 and CeO_2 phases coexisted with no other detectable impurities in Fe_2O_3@CeO_2 and Fe_2O_3@CeO_2–O_V samples (Fig. S2, ESI†).

Fourier-transform infrared (FT-IR) spectroscopy was applied to detect the surface functional groups, and the infrared spectra of Fe_2O_3@CeO_2–O_V, Fe_2O_3@CeO_2, Fe_2O_3, and CeO_2 (Fig. S3a, ESI†) samples were collected in the wavenumber range of 4000–500 cm^{-1}. Characteristic peaks are observed at 545 and 557 cm^{-1}, corresponding to the asymmetric tensile vibrations of Ce–O bonds and Fe–O, respectively. The vibrations at ~1643 and ~3440 cm^{-1} are attributed to OH^- groups in water, and the two peaks detected at ~1392 cm^{-1} and ~1564 cm^{-1} arising from the $-COO^-$ groups are attributed to dissolved atmospheric CO_2 and carboxylate in the ligand.[28] The formation of the Fe_2O_3–CeO_2 heterojunction structure was also confirmed *via* Raman spectroscopy (Fig. S3b, ESI†). For the CeO_2 sample, a distinct Raman band is observed at ~464 cm^{-1}, corresponding to the F_{2g} vibration of fluorite CeO_2. Characteristic Raman bands of Fe_2O_3 are present at 221, 289, 406 and 653 cm^{-1}. For the heterojunction samples, both bands from CeO_2 and Fe_2O_3 are observable, in accordance with the coexistence of the two phases from PXRD patterns. Broadening of the F_{2g} peak of CeO_2 after heterojunction formation is observed, indicating the increased structural distortion at the Fe_2O_3–CeO_2 heterojunction interface.[29] Notably, after the annealing process, the Raman peaks show a significant blue-shift for the defect-engineered Fe_2O_3@CeO_2–O_V sample, indicating the expansion of the lattice and decrease of crystallinity due to the introduction of abundant oxygen vacancies.

 This journal is © The Royal Society of Chemistry 2024

Open Access Article. Published on 14 kesäkuuta 2024. Downloaded on 13.5.2026 1.36.10.
This article is licensed under a Creative Commons Attribution-NonCommercial 3.0 Unported Licence.

The morphological evolution of the catalysts was analyzed by field emission scanning electron microscopy (FESEM). After the initial solvothermal reaction, ultrathin MIL-53 nanosheet arrays were covered on the NF substrate surface (Fig. S4, ESI†). Through the Ce-assisted templated hydrolysis of the MOF precursor during the secondary hydrothermal reaction, the nanosheet arrays of MIL-53 transformed into self-assembled nanoflower structures for the Fe_2O_3@CeO_2 heterojunction material (Fig. S5, ESI†). The hydrangea-like nanoflower microstructures with the scale around 1.5–3 μm comprised thin nanosheets with a thickness around 13 nm, endowing the material with hierarchical structures with abundant mass diffusion channels, integrated charge transport pathways and highly exposed active planes. Compared with the biphasic oxide materials derived from MOF precursor, the Fe_2O_3 sample directly from solution deposition (Fig. S6, ESI†) shows a similar vertically intergrown nanosheet array morphology with the MIL-53 precursor, while the CeO_2 sample without the addition of Fe sources presents thick and smooth nanoplate morphology (Fig. S7, ESI†). Both samples show the absence of hydrangea-like morphology, proving that both the MOF precursor and Ce^{4+} ions play essential roles in the formation of such delicate micro-nanostructures. After the final annealing process, defect-rich Fe_2O_3@CeO_2–O_V retained the nanoflower structure of Fe_2O_3@CeO_2 without obvious morphology change, confirming the integrity of the heterojunction backbone during defect engineering processing (Fig. 1c, d and Fig. S8, ESI†). To further investigate the detailed interfacial structure of the nano-heterojunction, transmission electron microscopy (TEM) was applied to analyze the microstructures of Fe_2O_3@CeO_2–O_V (Fig. 1e, f and Fig. S9, ESI†), in comparison with other samples (Fig. S10–S12, ESI†). As shown in the TEM images of various magnifications of Fe_2O_3@CeO_2–O_V, numerous ultrafine nanocrystals with sizes below 10 nm are randomly distributed on the intergrown nanosheets. A high-resolution TEM (HRTEM) image in Fig. 1g focusing on the boundary between the nanosheet and nanoparticle shows obvious lattice fringes of distinct orientations and spacings on the two sides of the boundary. The lattice fringes on the nanosheet side with 0.27 nm spacing are ascribed to the (104) plane of Fe_2O_3, and the (111) plane of CeO_2 with an interplanar distance of 0.31 nm is attributed to the lattice fringes on the nanoparticle side, in accordance with the selective area electron diffraction (SAED) patterns in Fig. S9f (ESI†), where diffraction rings corresponding to Fe_2O_3 (104) and CeO_2 (111) planes are observed. Formation of the Fe_2O_3–CeO_2 heterojunction was also evidenced by elemental mapping of the energy dispersive spectrometry (EDS) results (Fig. 1h and Fig. S13–S15, ESI†). Both metallic elements (Fe or Ce) and O show homogeneous distribution in CeO_2 (Fig. S13, ESI†) and Fe_2O_3 (Fig. S14, ESI†) samples, confirming their single-phase structures. In contrast, for the heterogeneous Fe_2O_3@CeO_2 (Fig. S15, ESI†) and Fe_2O_3@CeO_2–O_V (Fig. 1h), Fe and O are also homogeneously distributed throughout the materials, while Ce is located as randomly distributed high-concentration discrete islands, in agreement with the nanoparticle feature of the secondary CeO_2 phase on continuous Fe_2O_3 nanosheet substrates. Consequently, combined with diffraction, spectral and microscopic analyses, the successful construction of the Fe_2O_3–CeO_2 nano-heterojunction in the Fe_2O_3@CeO_2–O_V micro-nano-hydrangeas was confirmed in the form of highly-dispersed ultrafine CeO_2 nanoparticles imbedded onto Fe_2O_3 nanosheets.

XPS measurements were applied to investigate the surficial chemical states and charge transfer behaviors of the samples. From the survey spectra in Fig. S16 (ESI†), the surface of Fe_2O_3@CeO_2–O_V comprises elements such as Ce, Fe, O and C, consistent with the findings from EDS analysis. Signals of Ni are also detected from the NF substrates. The high-resolution O 1s spectrum of Fe_2O_3@CeO_2–O_V shows the presence of three types of oxides, M–O (529.6 eV), M–OH (531.7 eV) and adsorbed H_2O (533.5 eV). The surfaces of the heterojunction samples (Fe_2O_3@CeO_2–O_V and Fe_2O_3@CeO_2) resemble that of Fe_2O_3 (M–O at 529.8 eV) more than that of CeO_2 (M–O at 529.3 eV). The asymmetric nature of the M–OH peak indicates the presence of oxygen vacancies, and thus the peak ratio of M–OH/M–O could be applied for rough assessment of oxygen vacancy concentration. Noteworthily, for Fe_2O_3@CeO_2–O_V, the M–O signals are seriously weakened, while M–OH signals significantly strengthen together with adsorbed H_2O signals as compared with Fe_2O_3@CeO_2, suggesting abundant surficial oxygen vacancies. Also, all the O 1s peaks shift to higher bonding energy in the defect-rich sample, suggesting alleviation of M–O bonding strength. The Ce 3d spectrum of Fe_2O_3@CeO_2–O_V shows two sets of doublet peaks corresponding to Ce^{3+} (green peaks at 882.3, 886.1, 900.5, 907.4 and 904.9 eV) and Ce^{4+} (blue peaks at 883, 885.5, 889.2, 898.6, 901.1 and 917.4 eV),[30] while peaks corresponding to Ce^{3+} are not observed for CeO_2 and Fe_2O_3@CeO_2, which is ascribed to the spontaneous deoxygenation of Ce at high-temperature following the formula: $2Ce^{4+} + O_L^{2-} \leftrightarrow 2Ce^{3+} + O_V + 1/2O_2$, where the lattice oxygen O_L is released as oxygen gas to leave an oxygen vacancy. For the Fe 2p spectra of Fe_2O_3@CeO_2–O_V and Fe_2O_3@CeO_2, the case is much more complicated due to the overlap of Fe 2p signals with Ni and Ce Auger peaks (cyan Ni LMM and blue Ce MNN peaks in Fig. S16, ESI†) in binding energy.[31–33] After careful peak deconvolution, the Fe 2p spectrum of Fe_2O_3@CeO_2–O_V can be deconvoluted into a series of peaks: Fe^{2+} (green peaks, $2p_{3/2}$ at 711.2 eV, $2p_{1/2}$ at 724.3 eV, and satellite peak at 724 eV), and Fe^0 $2p^{3/2}$ (707 eV). Interestingly, the Fe^{3+} peaks observed in Fe_2O_3 and Fe_2O_3@CeO_2 are not observed for Fe_2O_3@CeO_2–O_V, while low-valence Fe states including Fe^{2+} and even metallic Fe(0) are present. These results confirm that the formation of low-valence Ce^{3+} and rich oxygen vacancies induces significant charge transfer and cross-interface electron density redistribution from the CeO_2 side to the Fe_2O_3 side of the heterojunction, leading to reduction of Fe centers. Formation of abundant oxygen vacancies was more directly confirmed by EPR as shown in Fig. 1i, where the strongest magnetic signals at g = 2.003 for Fe_2O_3@CeO_2–O_V indicated the highest concentration of unpaired electrons as compared with other samples, which were usually induced by oxygen vacancies.[34]

Open Access Article. Published on 14 kesäkuuta 2024. Downloaded on 13.5.2026 1.36.10.
This article is licensed under a Creative Commons Attribution-NonCommercial 3.0 Unported Licence.

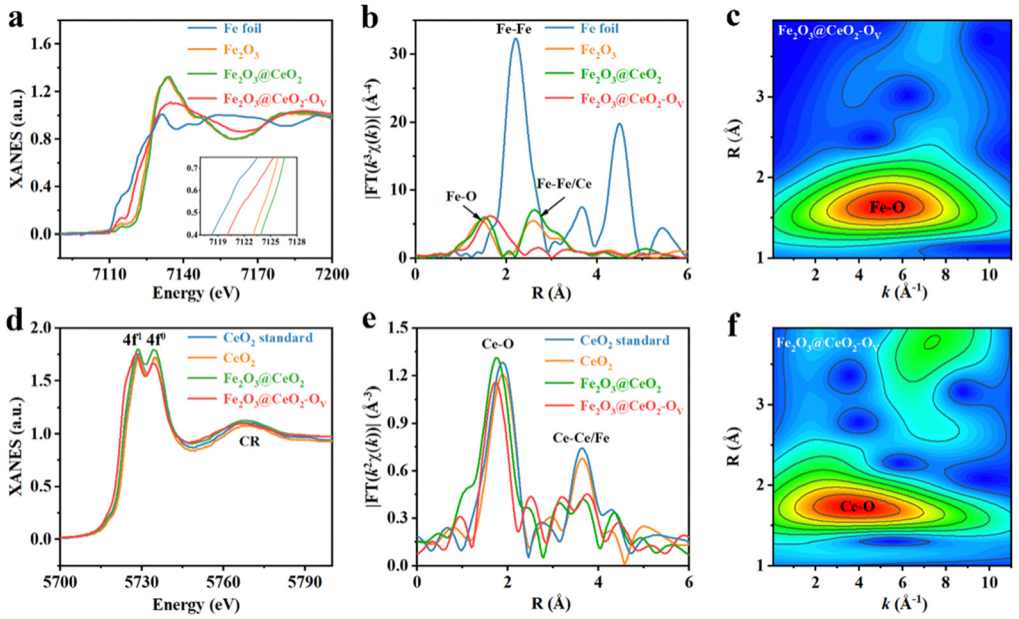

Fig. 2 XAFS characterization. (a) Fe K-edge XANES spectra and (b) Fourier-transformed k^3-weighted EXAFS spectra of Fe_2O_3@CeO_2–O_V, Fe_2O_3@CeO_2, Fe_2O_3 and Fe foil as reference. (c) WT-EXAFS contour plot of Fe K-edge signals of Fe_2O_3@CeO_2–O_V. (d) Ce L_3-edge XANES spectra and (e) Fourier-transformed k^2-weighted EXAFS spectra of Fe_2O_3@CeO_2–O_V, Fe_2O_3@CeO_2, CeO_2 and commercial CeO_2 as reference. (f) WT-EXAFS contour plot of Ce L_3-edge signals of Fe_2O_3@CeO_2–O_V.

The chemical states and the localized coordination environment of the samples were further investigated by XAFS spectroscopy. Fig. 2a shows the Fe K-edge X-ray absorption near-edge structures (XANES) profiles of Fe_2O_3@CeO_2, Fe_2O_3@CeO_2–O_V, Fe_2O_3 samples and Fe foil as references. The heterojunction Fe_2O_3@CeO_2 sample shows similar absorption curve shape and peak positions with the single-phase Fe_2O_3 sample, indicating that Fe in Fe_2O_3@CeO_2 mainly exists in the form of Fe^{3+} in FeO_6 octahedra.[35] After calcination, the defect-engineered Fe_2O_3@CeO_2–O_V shows an obvious shift of the absorption edge to lower energy, approaching that of Fe foil, indicating the decreased Fe valence state between Fe(0) and Fe(III), in accordance with the Ce-reduction-induced charge transfer from the CeO_2 side to the Fe_2O_3 side of the heterojunction from XPS results.[36] Also, Fe_2O_3@CeO_2–O_V shows a flattened white line peak at 7126.7 eV, with reduced white-line peak intensity compared with Fe_2O_3@CeO_2, corresponding to less electron transfer from Fe centers to nearby coordination atoms (O in this case), further probing the increase of localized structural disorder after defect engineering. Fig. 2b shows the Fourier-transformed Fe K-edge extended X-ray absorption fine structure (EXAFS) curves of all the samples. Compared with Fe foil, no Fe–Fe signals around 2.21Å are observed for the three samples, proving the absence of metallic Fe species. Two prominent peaks at 1.51 Å and 2.62 Å are observed for Fe_2O_3@CeO_2 and Fe_2O_3, which could be assigned to first-shell Fe–O and second-shell Fe–Fe/Ce, respectively. The increased intensity of the 2.62 Å peak for Fe_2O_3@CeO_2 could be attributed to the additional second-shell Fe–Ce interactions from heterojunction formation. The defect-rich Fe_2O_3@CeO_2–O_V however shows distinct EXAFS features. The first peak shifts to 1.75 Å with dramatic broadening, while the second peak almost disappears. Such obvious change is evident for the breaking of long-range ordered structures due to defect-induced lattice distortion and amorphization. Quantitative EXAFS fitting analyses were performed for all the samples to investigate the coordination configuration, where the structural parameters are listed in Table S1 (ESI†) (original and fitting curves of separated samples in both k and R spaces are given in Fig. S17, ESI†). Both Fe_2O_3 and Fe_2O_3@CeO_2 adopt a typical Fe_2O_3-typed coordination structure with 6 first-shell Fe–O and 12 second-shell Fe-Fe coordination numbers, while the Fe–O coordination number of Fe_2O_3@CeO_2–O_V decreases to ~5.0, with expanded Fe–O bond length from 1.99 Å to 2.07 Å, and signals from second-shell almost disappear, confirming the formation of abundant oxygen vacancies and increased structural disorder. A wavelet transform (WT) of Fe K-edge EXAFS signals for Fe_2O_3@CeO_2–O_V is displayed in Fig. 2c, showing only one intensity maximum at ~5.26 Å^{-1} in k space, which expands to a higher R region as compared with that of Fe_2O_3 and Fe_2O_3@CeO_2 (Fig. S18, ESI†), attributed to extended Fe–O backscattering contribution.[37]

Fig. 2d shows the Ce L_3-edge XANES profiles of Fe_2O_3@CeO_2, Fe_2O_3@CeO_2–O_V and CeO_2, together with a commercial CeO_2 sample as the Ce standard. Two white-line edge absorption peaks at 5728.7 eV and 5734.2 eV are identified, corresponding to a transition from the Ce $2p_{3/2}$ state to unoccupied Ce 5d states mixed with $4f^1$ or $4f^0$ final states, confirming the coexistence of Ce^{3+}/Ce^{4+} mixed oxidation states. The white-line edge of Fe_2O_3@CeO_2–O_V is located at the lowest energy, accompanied by decreased intensity of the $4f^0$ edge, indicating the lowered Ce valence and increased Ce^{3+}/Ce^{4+} ratio due to the formation of increased oxygen vacancies. The continuum

 This journal is © The Royal Society of Chemistry 2024

Open Access Article. Published on 14 kesäkuuta 2024. Downloaded on 13.5.2026 1.36.10.
This article is licensed under a Creative Commons Attribution-NonCommercial 3.0 Unported Licence.

resonance (CR) bulk peak is attributed to the combination of Ce–Fe/Ce scattering. The Ce L_3-edge EXAFS spectra of all the Ce-containing samples are shown in Fig. 2e, which show two main features. The major peak around 1.75 Å is related to first-shell Ce–O coordination, as confirmed by quantitative EXAFS curve fitting (Fig. S19 and Table S2, ESI†). Notably, additional Ce–O scattering paths are fitted, with longer bond lengths than the typical Ce–O bonds in CeO_2 with lengths between 2.2 and 2.3 Å for both Fe_2O_3@CeO_2 and Fe_2O_3@CeO_2–O_V, hinting the contributions from interfacial Fe–O–Ce signals. Interestingly, the defect-rich Fe_2O_3@CeO_2–O_V shows decreased first-shell Ce–O coordination number of ~6.2; however with increased coordination from the extended 3.16 Å Ce–O bond, arising from the stronger adhesion of the CeO_2 nanoparticles to the Fe_2O_3 nanosheet surface due to oxygen-vacancy-induced evolution of atomic configuration, as later discussed in the calculation part. The second peak should be related to the second-nearest Ce–Ce or Ce–Fe scattering, and the slight change of shape in this peak contains fingerprint information indicative of redistributed middle-range lattice structures due to heterojunction and defect formation, respectively. The WT-EXAFS contour plot of Fe_2O_3@CeO_2–O_V in Fig. 2f and Fig. S20 (ESI†) shows an intensity maximum expanded between 2 and 6 $Å^{-1}$ in k space, attributed to contributions from various Ce–O backscattering of varying bond lengths. A weaker peak from Ce–Ce/Fe backscattering signals is also identified in the high R region. Defect-induced structural variation was also validated by X-ray pair-distribution function (PDF) analyses. As shown in Fig. S21 (ESI†), the PDF profiles of Fe_2O_3@CeO_2–O_V and Fe_2O_3@CeO_2 mostly resemble that of CeO_2 instead of Fe_2O_3, possibly owing to the high surface coverage of CeO_2 nanoclusters and the low crystallinity of the Fe_2O_3 substrates. Simulation reveals that the first three peaks of both Fe_2O_3@CeO_2–O_V and Fe_2O_3@CeO_2 could be attributed to Ce–O, O–O and Ce–Ce of CeO_2, respectively (Fig. S22, ESI†). For Fe_2O_3@CeO_2–O_V, the Ce–Ce and Ce–O peaks are enhanced, while the O–O peak intensity decreases as compared with Fe_2O_3@CeO_2, in accordance with the lower Ce–O coordination numbers from EXAFS results, indicating the loss of lattice oxygen and formation of oxygen vacancies upon the defect engineering process.[30,38]

The electrochemical water oxidation performance of all the samples was further evaluated in a three-electrode system in 1.0 M KOH alkaline aqueous media. Fig. 3a shows the back-scan linear sweep voltammetry (LSV) OER polarization curves with 90% iR-correction manually compensated. Among all the samples, the defect-engineered heterojunction electrode Fe_2O_3@CeO_2–O_V exhibits the lowest overpotential of 172 mV and 201 mV to attain current densities of 10 and 100 mA cm^{-2}, respectively, dramatically outperforming that of Fe_2O_3@CeO_2

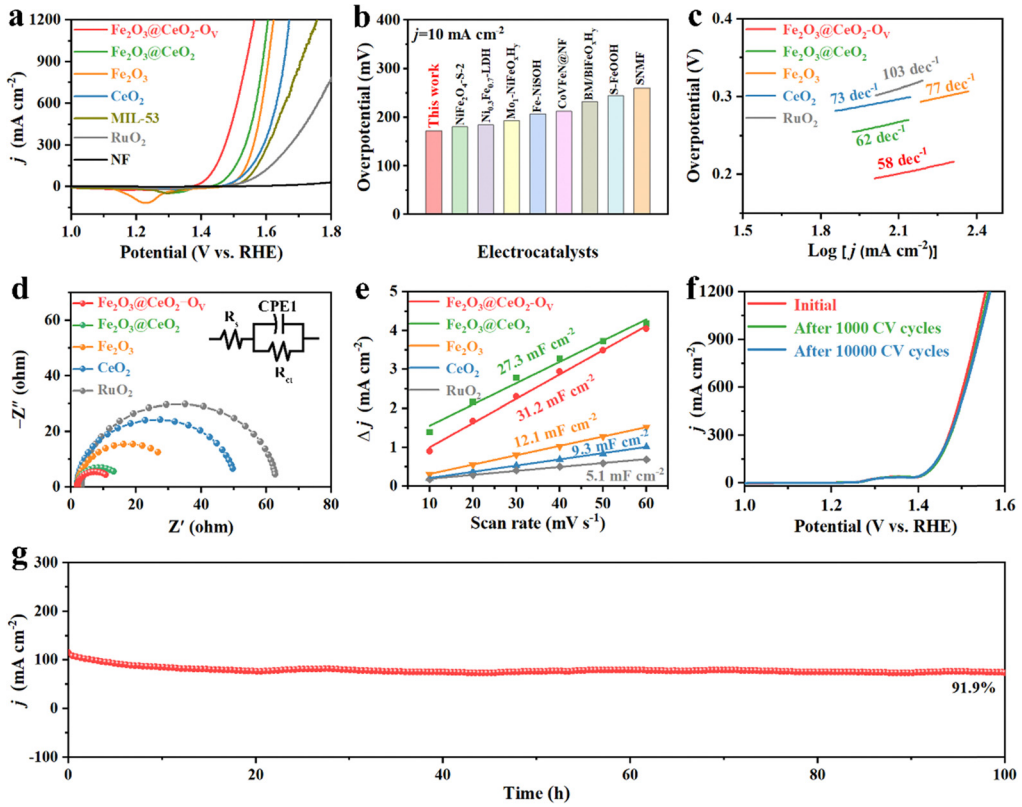

Fig. 3 OER performance of the prepared electrodes. (a) LSV negative scan curves in 1.0 M KOH with 90%-iR compensation. (b) Comparison of overpotentials at a current density of 10 mA cm^{-2} with reported Fe-based electrocatalysts. (c) Corresponding Tafel plots. (d) EIS plots of samples, and the insert shows the equivalent circuit. (e) C_{dl} calculations of the Fe_2O_3@CeO_2–O_V, Fe_2O_3@CeO_2, Fe_2O_3, CeO_2 and RuO_2 samples. (f) LSV curves of Fe_2O_3@CeO_2–O_V, before and after 1000 and 10 000 CV cycles in 1.0 M KOH for the OER. (g) Chronoamperometric stability tests of Fe_2O_3@CeO_2–O_V.

Open Access Article. Published on 14 kesäkuuta 2024. Downloaded on 13.5.2026 1.36.10.
This article is licensed under a Creative Commons Attribution-NonCommercial 3.0 Unported Licence.

(217 and 261 mV), Fe_2O_3 (252 and 297 mV), CeO_2 (242 and 306 mV), MIL-53 (268 and 326 mV) and commercial RuO_2 (187 and 296 mV). Fe_2O_3@CeO_2–O_V also performs excellently under large current conditions, requiring only 317 mV to reach 1000 mA cm^{-2} current density, a typical condition for industrial electrolyzers. Such pronounced performance outperforms those of most of the reported Fe-based oxide/hydroxide/oxyhydroxide materials and those of even many noble-metal-based catalysts, as shown in Fig. 3b and Table S3 (ESI†). Tafel slope values were calculated to understand the intrinsic kinetics of catalysts. As shown in Fig. 3c, Fe_2O_3@CeO_2–O_V shows the lowest Tafel slope of 58 mV dec^{-1} among all the samples, lower than Fe_2O_3@CeO_2 (62 mV dec^{-1}), Fe_2O_3 (73 mV dec^{-1}) and CeO_2 (77 mV dec^{-1}), and notably also lower than RuO_2 (103 mV dec^{-1}), proving the promoting synergistic effects of abundant heterojunction interfaces and oxygen defects. Electrochemical impedance spectroscopy (EIS) measurements were applied to investigate the charge transfer behaviors of samples. From the Nyquist plots in Fig. 3d, the heterojunction Fe_2O_3@CeO_2 shows a charge-transfer resistance (R_{ct}) of 13.09 Ω, much lower than that of single-component Fe_2O_3 (26.71 Ω) and CeO_2 (49.72 Ω), confirming that the formation of heterojunction significantly increases the charge transfer owing to interfacial charge redistribution. Defect engineering further modulated the electronic structure of the heterojunction and improved the conductivity, where defect-rich Fe_2O_3@CeO_2–O_V presented the lowest R_{ct} of 10.66 Ω, indicating the fast electron transfer between the electrode–electrolyte interfaces. It is also worth mentioning that the *in situ* grown electrodes exhibit much lower R_{ct} than commercial RuO_2 simply loaded onto the NF substrate (79.44 Ω), further proving the advantage of our self-supporting electrodes with hierarchical structures and interconnected conductive networks.

Electrochemical surface area (ECSA) is an important criterion to represent the density of intrinsic surface active sites of catalysts. The ECSA values were calculated accordingly as proportional to the electrochemical double-layer capacitance (C_{dl}) in Fig. 3e. C_{dl} values were calculated from cyclic voltammetry (CV) scans of different scan rates (10, 20, 30, 40, 50 and 60 mV s^{-1}) in the non-redox region, as shown in Fig. S23 (ESI†). Fe_2O_3@CeO_2–O_V has the highest C_{dl} value of 31.2 mF cm^{-2}, followed by Fe_2O_3@CeO_2 (27.3 mF cm^{-2}), Fe_2O_3 (12.1 mF cm^{-2}), and CeO_2 (9.3 mF cm^{-2}), confirming that the formation of the heterojunction and following defect engineering effectively increase the number of surficial active sites. These results are also supported by the geometric surface areas calculated using the Brunauer–Emmett–Teller (BET) method from 77 K N_2 sorption isotherms, as presented in Fig. S24 (ESI†), where Fe_2O_3@CeO_2–O_V shows the highest BET area of 75.44 m^2 g^{-1}. The OER LSV polarization curves were further normalized by using calculated ECSAs to exclude the influence of structural and geometrical variations of electrodes and present the intrinsic catalytic activities of samples (Fig. S25, ESI†). After ECSA-normalization, the superiority of Fe_2O_3@CeO_2–O_V over other samples becomes even more pronounced with a much lower OER onset, requiring only 226 mV to reach a current density of 10 mA cm^{-2} ECSA, which is significantly higher those of than commercial RuO_2 (0.1136 mA cm^{-2} ECSA) at the same overpotential. The high intrinsic activity of Fe_2O_3@CeO_2–O_V for OER catalysis was further determined by calculating the turn-over frequency (TOF) values of singular active sites under certain given potentials. TOF values were estimated from the redox peaks of transition metals in CV scans of different scan rates, assuming a one-electron process for oxidation of metal centers (Fig. S26, ESI†). Fe_2O_3@CeO_2–O_V shows the highest TOF values of 0.05, 0.18 and 0.431 s^{-1} at overpotentials of 200, 250 and 300 mV, predominantly higher than those of other samples. These combined analyses provide solid evidence that construction of heterojunction nanostructures and the following defect engineering process could enhance interfacial charge transfer and increase both the catalytic active surface areas and intrinsic catalytic activities of singular active sites by effective modulation of interfacial geometric and electronic structures.

Stability and durability are essential concerns for industrial applications. Industrial water splitting electrolyzers work under harsh conditions, thus requiring the electrodes to endure extreme chemical, electrochemical and mechanical corrosions from highly alkaline media, high current and vigorous shock of generated gas bubbles. Fig. S27 (ESI†) shows a multiple current step chronopotentiometry (MCSCP) curve of Fe_2O_3@CeO_2–O_V, where the current density step increment was set as 4 mA cm^{-2}. As the current densities stepped, the potential immediately responded and stabilized, remaining mostly constant for 500 seconds. Such rapid response to current change and rapid equilibrium are indicative of the fast mass diffusion at the electrode surface, owing to the hierarchical three-dimensional nanoflower structures. These properties could enable the quick start and rapid response of the electrodes when utilized in industrial water electrolyzers, especially powered by a green-electricity power source (like solar panels or wind turbos) with unstable power supply. Accelerated degradation tests (ADT) were further conducted *via* CV cycling within the potential window of 1.20 to 1.50 V. As shown in Fig. 3f, the LSV curves remain mostly unchanged after ADT cycling, where the overpotential required to reach the current density of 100 mA cm^{-2} shows negligible change. Even up to a high current density of 1000 mA cm^{-2}, the overpotential after 10 000 CV cycles increases by only 9 mV, proving the structural and chemical stability of Fe_2O_3@CeO_2–O_V against varying current–potential conditions. SEM images of Fe_2O_3@CeO_2 and Fe_2O_3@CeO_2–O_V after ADT tests (Fig. S28, ESI†) show that the hierarchical hydrangea-like nanoflower microstructures assembled from nanosheets were mostly well-retained, proving the excellent structural stability of the heterojunction samples against long-term electrochemical corrosion and mechanical wear. Chronoamperometric measurements under constant potentials were applied to access the steady-state long-term stability of the electrodes. The Fe_2O_3@CeO_2–O_V electrode could maintain the current density around 10 and 100 mA cm^{-2} for continuous 100 h at constant potentials of 1.424 and 1.509 V, respectively, with only minor current fluctuation and degradation (Fig. 3g and Fig. S29, ESI†). After 100 h of electrolysis at 1.509 V,

 This journal is © The Royal Society of Chemistry 2024

Open Access Article. Published on 14 kesäkuuta 2024. Downloaded on 13.5.2026 1.36.10.
This article is licensed under a Creative Commons Attribution-NonCommercial 3.0 Unported Licence.

the electrode could still retain 91.9% of the starting current density. XRD, Raman (Fig. S30, ESI†) and XPS (Fig. S31, ESI†) analyses after OER tests further confirm no significant change of the crystalline structure and elemental composition for Fe_2O_3@CeO_2–O_V. Specifically, an obvious blueshift of the CeO_2 F_{2g} peak is observed, corresponding to lattice expansion due to the formation of additional oxygen vacancies and surficial reconstruction during the reaction. The hierarchical micro–nano structure of the heterojunction is also well-retained without obvious morphology change, as confirmed by the SEM (Fig. S32, ESI†), TEM and HRTEM images (Fig. S33, ESI†) after OER testing. These results confirm that the Fe_2O_3@CeO_2–O_V electrocatalyst could operate steadily under both rapidly varying current–voltage conditions and long-term steady-state electrolysis, especially under industrial-level high current densities, thus presenting excellent stability and durability. Selectivity is another critical index for practical applications. Incomplete oxidation of water through the two-electron pathway into hydroperoxide (H_2O_2) may lead to corrosion of the polymeric components of the membrane electrode assembles (MEAs) through Fenton-like reaction, together with other undesirable side reactions. The Faraday efficiency (FE) of Fe_2O_3@CeO_2–O_V was thus evaluated *via* the rotating ring-disk electrode (RRDE) experiments in N_2-saturated 1.0 M KOH solution. To confirm that the current was induced by water oxidation instead of side effects, a constant potential of 0.45 V was applied on the Pt ring electrode to reduce any oxygen generated at the disk electrode loaded with the Fe_2O_3@CeO_2–O_V electrocatalyst. As shown in Fig. 4a, both disk and ring currents are negligible until the oxygen evolution potential is reached at the disk electrode, and both increase concurrently as the potential further increases to a higher level. The FE at 1.55 V is calculated to be as high as 96.3%, indicating that water is completely oxidized into oxygen with negligible side reactions. The FE measurement was double-checked using a conventional water drainage method. At constant current densities of 100 mA cm^{-2} and 500 mA cm^{-2}, the oxygen evolution rates were measured to be 0.09 and 0.18 mL min^{-1}, respectively, corresponding to FEs of 99.99% and 99.92%, respectively (Fig. 4b). The actual oxygen production rates at different times are close to theoretical values, and the calculated FE values approach 100%, again validating the complete four-electron water oxidation of the defect-engineered heterojunction electrodes. Considering the excellent OER catalytic activity and stability of Fe_2O_3@CeO_2–O_V electrodes, we further applied the self-supporting electrodes in a two-electrode MEA-based flow cell to examine the overall water splitting performance under industrial conditions. The schematic diagram and photographic image of the testing cell are given in the insert in Fig. 4c and Fig. S34 (ESI†). The self-supporting Fe_2O_3@CeO_2–O_V electrode with the NF substrate was directly used as the anode, and a carbon paper loaded with a commercial Pt/C catalyst was used as the cathode, and both electrodes were pressed tightly against an anion exchange membrane. The 1.0 M KOH solution electrolyte flowed through the anode chamber. The MEA-based water splitting performance was validated using the potential-scan polarization curve, as shown in Fig. 4d. The cell shows promising performance, requiring a low cell voltage of 1.61 V and 1.80 V to reach current densities of 100 and 500 mA cm^{-2}, respectively. The flow cell specifically demonstrates great potential in the high current density region, reaching 1000 mA cm^{-2} at a cell voltage of 1.93 V. When a current density of 1.0 A cm^{-2} was applied for 100 h, the cell operated steadily, with the cell voltage increasing from the initial 1.968 V to 2.019 V, exhibiting favorable stability. These results demonstrate the promising performance and stability of the defect-engineered Fe_2O_3@CeO_2–O_V heterojunction self-supporting

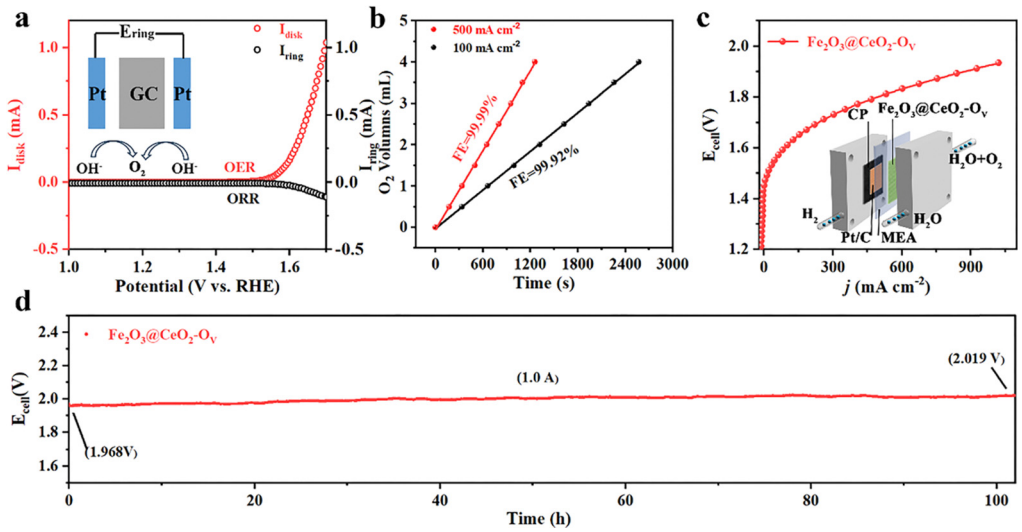

Fig. 4 OER performance of the prepared electrodes. (a) RRDE testing results. The O_2 generated at the disk electrode loaded with the Fe_2O_3@CeO_2–O_V catalyst was reduced at the Pt ring electrode at a constant potential of 0.45 V (*vs.* RHE) in N_2-saturated 1.0 M KOH solution. (b) Oxygen evolution rates at constant current densities of 100 and 500 mA cm^{-2}, respectively. (c) Overall water splitting performance of the Fe_2O_3@CeO_2–O_V anode coupled with the commercial Pt/C cathode in a membrane-based flow cell. (d) Chronopotentiometric curve of the Fe_2O_3@CeO_2–O_V‖Pt/C flow cell for overall water electrolysis for 100 h. Constant current densities of 1.0 A cm^{-2} were applied during the reaction.

Open Access Article. Published on 14 kesäkuuta 2024. Downloaded on 13.5.2026 1.36.10.
This article is licensed under a Creative Commons Attribution-NonCommercial 3.0 Unported Licence.

electrodes in the industrial membrane-based electrolyzer under high current working conditions.

The large number of oxygen vacancies and outstanding OER performance of Fe_2O_3@CeO_2–O_V, especially the much lower OER onset potential and Tafel slop, indicate the substantial change of reaction kinetics and possible involvement of lattice oxygen. To identify the reaction pathway, the pH-dependence of the electrodes was evaluated. LSV curves were collected under different pH values ranging from 12.5 to 14 (Fig. 5a and Fig. S35, ESI†). Fe_2O_3@CeO_2–O_V shows much stronger pH dependence than Fe_2O_3@CeO_2 and other comparison samples. To quantify the pH dependence of OER activity, the proton reaction orders on RHE scale (ρ^{RHE}, $\rho^{RHE} = \partial \log(j)/\partial pH$) were derived, which reflected the relationship between the OER reaction kinetics and proton activity. The ρ^{RHE} value (Fig. S36, ESI†) of Fe_2O_3@CeO_2–O_V is fitted to be 0.90, larger than that of Fe_2O_3@CeO_2 (0.68), corresponding to a stronger pH-dependence, which implies non-cooperative proton-electron transfer and a LOM pathway rather than the conventional AEM during the OER.[39] Generation of negatively charge oxygen-containing species ($*O_2^{2-}$ and $*O_2^-$) is another important feature of the LOM-based OER, thus detection of these intermediate species provides solid evidence of surficial oxygen involvement. Tetramethylammonium hydroxide (TMAOH) is a typical detector because the tetramethylammonium cation (TMA^+) could bind strongly with the oxygen-containing species through electrostatic interaction and compete with the OER, thus hindering the OER kinetics. The KOH electrolyte was then replaced with the TMAOH solution for OER testing to verify the reaction mechanism. Fe_2O_3@CeO_2–O_V shows significant OER activity reduction, where the overpotential to reach 100 mA cm^{-2} current density increases by 192 mV, indicative of combination between TMA^+ and negatively charged oxygen species, implying a LOM pathway. Comparatively, the reaction activity reduction of Fe_2O_3@CeO_2 is not so pronounced, and the corresponding overpotential increment is only 128 mV, corresponding to an AEM mechanism.[40] Variation of the pre-OER redox peaks and pseudocapacitive currents from CV plots under different scan rates (1 to 5 mV s^{-1}) could be applied to study the OER kinetics (Fig. S37, ESI†). The relationship between the current (i) and sweep rate (ν) follows the equation: $i = a\nu^b$, where the b value could be acquired as the slope from the linear fitting of $\log(i)$ against $\log(\nu)$, and applied to elucidate the reaction mechanism. Specifically, the b value of 0.5 represents a completely diffusion-controlled process, whilst 1.0 indicates an ideal surficial capacitive process. The b value of Fe_2O_3@CeO_2–O_V is calculated to be 0.843, in contrast to the 0.506 for Fe_2O_3@CeO_2, revealing that the OER reaction transforms from a typical diffusion-dominated process for Fe_2O_3@CeO_2 into a majorly surface-controlled one. More specifically, the contribution from either surficial capacitive or diffusion component at a fixed potential V is quantified using the following formula: $i(V) = k_1V + k_2V^{1/2}$, where k_1V is attributed to the capacitance portion, and $k_2V^{1/2}$ is the diffusion fraction. As shown in Fig. 5b and c, the pseudocapacitive behavior contributes to most of the current densities for Fe_2O_3@CeO_2–O_V, especially at higher scan rates, contributing 70% of the redox current at a scan rate of 5 mV s^{-1}, higher than that of Fe_2O_3@CeO_2 (64%) under the same condition. The pseudocapacitive charging process of transition metal compounds is often related to the formation of abundant active centers at anodic potentials lower than the OER onset, thus boosting the following OER process.[41,42]

The above results provide abundant yet indirect evidence of the LOM pathway during the OER process for Fe_2O_3@CeO_2–O_V. To directly reveal the participation of lattice oxygen during the OER process, we performed operando isotopic ^{18}O-labeled

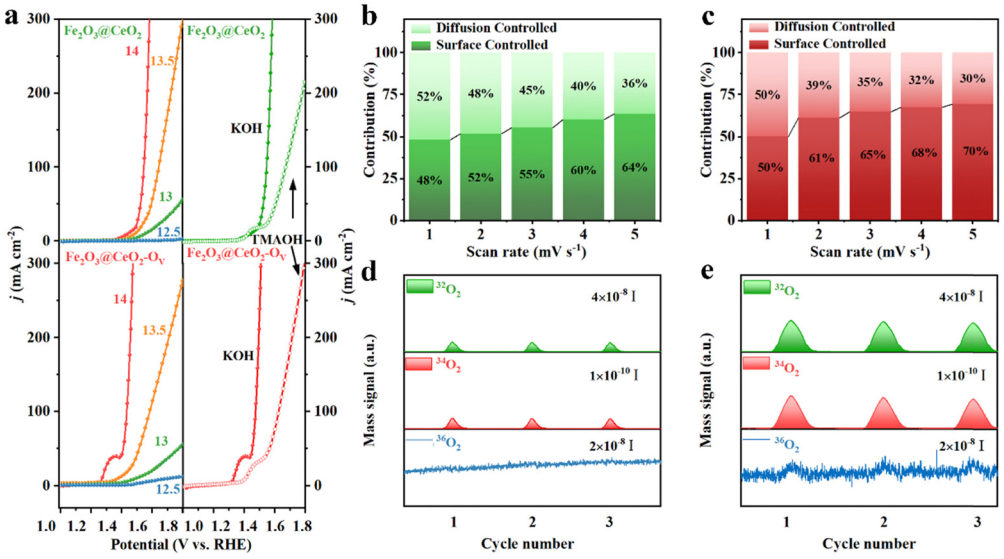

Fig. 5 OER performance of the prepared electrodes. (a) LSV curves of Fe_2O_3@CeO_2–O_V and Fe_2O_3@CeO_2 under different pH conditions (left) and in 1.0 M KOH or 1.0 M TMAOH, respectively (right). Contribution ratios of the capacitive and diffusion-controlled current densities *vs.* scan rates for (b) Fe_2O_3@CeO_2 and (c) Fe_2O_3@CeO_2–O_V. DEMS results by ^{18}O-isotopic labeling experiments for (d) Fe_2O_3@CeO_2 and (e) Fe_2O_3@CeO_2–O_V.

 This journal is © The Royal Society of Chemistry 2024

Open Access Article. Published on 14 kesäkuuta 2024. Downloaded on 13.5.2026 1.36.10.
This article is licensed under a Creative Commons Attribution-NonCommercial 3.0 Unported Licence.

differential electrochemical mass spectrometry (DEMS) experiments for both Fe_2O_3@CeO_2–O_V and Fe_2O_3@CeO_2. The working electrodes were firstly labeled by CV scanning in ^{18}O-labeled 0.1 M KOH solution, where the surficial oxygen atoms would be exchanged by ^{18}O if the LOM pathway was possible. The labeled electrodes were then tested for the OER by CV in 0.1 M KOH solution with regular H_2O, and the gases generated were constantly monitored using mass spectra. Fig. 5d and e show the acquired DEMS spectra from three consecutive scans for Fe_2O_3@CeO_2 and Fe_2O_3@CeO_2–O_V, respectively. Mass signals at m/z = 32, 34 and 36 were monitored, corresponding to $^{16}O_2$, $^{16}O^{18}O$, and $^{18}O_2$ in the gas products during potential scans. As shown in Fig. S38 (ESI†), during the ^{18}O-labeling process, obvious $^{18}O_2$ signals were observed from the OER of $H_2{}^{18}O$, and some $^{16}O^{18}O$ signals were also recorded due to surface oxygen exchange. Notably, for Fe_2O_3@CeO_2–O_V, some minor signals of $^{16}O_2$ were also detected, corresponding to the release of two adjacent surface oxygen atoms through a dual-vacancy LOM pathway, which was absent for Fe_2O_3@CeO_2. The participation of surface oxygen was further proven by measuring the labeled electrodes in $H_2{}^{16}O$, where Fe_2O_3@CeO_2–O_V showed both signals from $^{16}O^{18}O$ and $^{18}O_2$, confirming the exchange and release of surface oxygen atoms during the OER. Similarly, the signals from $^{18}O_2$ were negligible from the background noise for Fe_2O_3@CeO_2.

Conclusively, the DEMS results confirmed the production of LOM-related isotopic-labeled gas products, thus proving the involvement of surface oxygen atoms during the OER for the defect-engineered Fe_2O_3@CeO_2–O_V.[12,19,43,44] To further understand the promoting effect of oxygen vacancies towards the OER for the defect-engineered Fe_2O_3@CeO_2–O_V, DFT+U calculations were implemented. The model of Fe_2O_3@CeO_2–O_V is established as a $Ce_{10}O_{20}$ cluster supported on the α-Fe_2O_3 (104) surface, as characterized by XRD in Fig. 1b. As shown in Fig. S39 (ESI†), the CeO_2 favors to bind on the Fe-terminal surface of α-Fe_2O_3 instead of the O-terminal one. By comparing the oxygen vacancy (O_V) formation energies of different situations, O_V is found to preferably form on top of the CeO_2 cluster, rather than at the heterojunction interface or on top of the Fe_2O_3 substrate, in accordance with the observed spontaneous deoxygenation of CeO_2 upon heat treatment. After achieving the representative configurations of Fe_2O_3–CeO_2 heterojunction catalysts without and with O_V, the reaction pathway following the LOM was explored. Fig. S40 (ESI†) shows the corresponding geometric configurations of reaction intermediates for both catalysts. Interestingly, the already-existing O_V (denoted by the blue dashed circle) does not serve directly as the reaction active site for the LOM, but instead plays the role of a modulator to activate another lattice oxygen (O_L, the blue sphere), which combines with an adsorbed oxygen from solvent water (the purple sphere in Fig. 6a) to give out a molecule of O_2, leaving an additional instantaneous oxygen vacancy (*□). The free energy diagram in Fig. 6a shows the superior activity of Fe_2O_3@CeO_2–O_V with the lower free energy increasing as

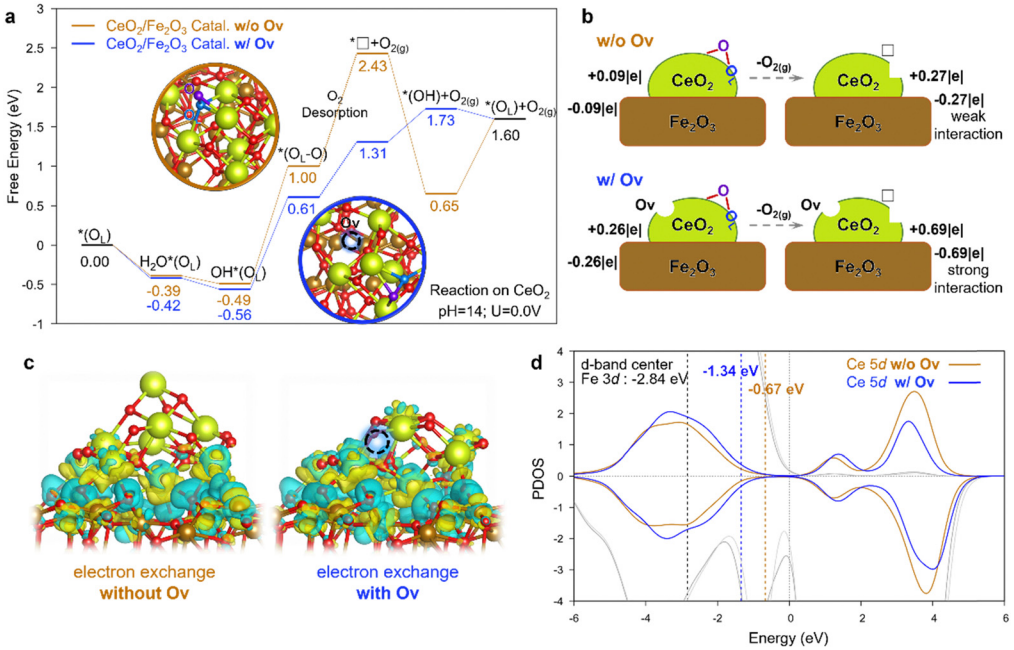

Fig. 6 DFT calculations for LOM-based OER catalyzed by the Fe_2O_3@CeO_2–O_V and Fe_2O_3@CeO_2 catalysts. (a) Free energy diagram for LOM-based OER steps. The detailed 3D configurations are shown in Fig. S40 (ESI†). Color code: Ce in yellow; Fe in brown; the O about to be removed in LOM in blue; the O from water in purple; the other O in red. The dotted lines represent the O_2 desorption step. (b) Illustration of Bader charge changes during the O_2 desorption step. (c) Charge density diagram showing the electron exchange between the CeO_2 cluster and Fe_2O_3 support of the *□ intermediate after O_2 desorption. Electron depletion and accumulation are depicted by yellow and blue areas, respectively. The isosurfaces are plotted at the value of ± 0.03 |e| $Å^{-3}$. (d) Projected density of states (PDOS) of Ce 5d orbitals in the *□ intermediate of CeO_2/Fe_2O_3 catalysts. The lighter and darker gray lines show the PDOS of surface Fe atoms with and without O_V on CeO_2, respectively. The yellow and blue numbers show the d-band-center of Ce without and with O_V.

Open Access Article. Published on 14 kesäkuuta 2024. Downloaded on 13.5.2026 1.36.10.
This article is licensed under a Creative Commons Attribution-NonCommercial 3.0 Unported Licence.

compared with Fe_2O_3@CeO_2 under standard basic conditions (pH = 14 and U = 0 V). The overpotential of the catalyst with O_V, as determined in the step of O_L–O formation ($OH^*(O_L)$ + $OH^- \rightarrow *(O_L\text{–}O) + H_2O + e^-$), is lowered by 0.32 V when O_V was introduced. More importantly, without O_V, the Fe_2O_3@CeO_2 catalyst suffers from the extremely endergonic free energy of 1.43 eV during the O_2 desorption ($*(O_L\text{–}O) \rightarrow *\square + O_{2(g)}$), while the free energy increase dramatically lowers to 0.70 eV in the presence of O_V. Considering that this O_2 desorption is the key step in the LOM that can hardly be accelerated by the applied electro-potential, this result shows the counter-intuitive factor that the presence of a first O_V could promote the O_2 release to form another instantaneous oxygen vacancy $*\square$ during the catalytic cycle, thus promoting OER activity. For comparison, we also evaluated the cases where LOM-active sites were located at the heterojunction interface with and without O_V (Fig. S41, ESI†). The free energy diagram (Fig. S42, ESI†) confirms the promotion effect of a starting Ov at the interfacial site, but its activity is still inferior to that on top of CeO_2 in Fig. 6a. These results imply the actual active sites to be on top of the CeO_2 nanoparticles instead of on the Fe_2O_3 surface or at the CeO_2/Fe_2O_3 interface.

To figure out the chemistry behind, the Bader charge analysis was performed (Fig. 6b). For Fe_2O_3@CeO_2, when in contact with the Fe_2O_3 surface, the CeO_2 cluster without O_V takes a slightly positive charge (+0.09|e|), and the Fe_2O_3 surface is negative, indicating the electron transfer from CeO_2 to Fe_2O_3, in consistent with experimental results. After O_2 desorption, the positive charge of the CeO_2 cluster is increased by 0.18|e| (*i.e.* a total of 0.27|e|). For Fe_2O_3@CeO_2–O_V with the presence of a starting O_V, the CeO_{2-x} cluster is more positive (+0.26|e|), and this charge dramatically increases by 0.43|e| after O_2 desorption. The more significant charge polarization indicates the stronger interaction between the CeO_2 cluster and Fe_2O_3 support. This trend could also be observed from the charge density distribution plot in Fig. 6c showing the electron exchange at the heterojunction interface. The cluster/support interaction is so strong for the $*\square$ intermediate with O_V that the CeO_{2-x} cluster slightly changes its geometric configuration to take a closer contact with the support, like "butter soften on a hot pan". The effect of strong cluster/support interaction can also be elucidated by the projected density of states (PDOS) and d-band center in Fig. 6d. Due to the presence of O_V, the PDOS of Ce 5d shifts to a lower energy to better bind with Fe_2O_3. The d-band center of the Ce 5d orbital decreases from −0.67 eV to −1.34 eV when introducing the O_V, which becomes more closer to the d-band center of Fe 3d orbitals (−2.84 eV). Upshift of the O 2p band center is generally believed to be a key parameter to index the reactivity of lattice oxygen.[45,46] In our case, however, the situation is more complicated since two different metal d-bands coexist due to the formation of the oxide-heterojunction, and the strong cluster/support interaction would induce not only the modulation of electronic structures but also the geometric configuration, as was observed at the metal/oxide interface.[47,48] The PDOS of 2p orbitals of O on the CeO_2 cluster was also analyzed, as shown in Fig. S43 (ESI†). Without the starting O_V for Fe_2O_3@CeO_2, the O 2p moves closer to the Fermi level during the O_2 dissociation of the LOM, indicating the reduction of the CeO_2 cluster and the formation of Ce(III). In contrast, for Fe_2O_3@CeO_2–O_V with the presence of O_V, the O 2p moves away from the Fermi level during the O_2 dissociation of LOM due to the stronger electron interaction between the CeO_2 cluster and the Fe_2O_3 support, which compensated the effect from O_2 dissociation. (See detailed discussion after Fig. S43 in the ESI†). In general, the strong interaction between CeO_{2-x} and Fe_2O_3 cancels out part of the free energy raise of the additional instantaneous oxygen vacancy (*i.e.* $*\square$) during the O_2 desorption in LOM by boosting electron transfer from CeO_{2-x} to Fe_2O_3, thus contributing to the superior OER catalytic activity. One can postulate that such strong interaction at the heterojunction interface could promote the LOM in the OER over similar reducible oxide-heterojunction catalysts,[49,50] the mechanism of which can be helpful for the design of new LOM electrocatalysts.

Conclusions

In summary, we demonstrated a defect-engineered Fe_2O_3@CeO_2–O_V nano-heterojunction material as highly efficient self-supporting alkaline OER electrocatalysts. The electrodes exhibited superior OER activity and durability, especially under industrial large-current density conditions and membrane-based flow cells. ^{18}O-isotopic labelling experiments combined with a series of electrochemical measurements confirmed the participation of lattice oxygen, transforming the OER mechanism from the AEM to LOM. XPS, XAFS and DFT+U calculations revealed that oxygen vacancies predominantly existed on the surface of CeO_2 nanoclusters, inducing strong charge transfer from CeO_2 to Fe_2O_3 and electron density redistribution across the heterojunction interface. The presence of O_V on CeO_2 promoted strong cluster/support interaction and downshifted the Ce 5d band center closer to the Fe 3d bands, lowering the free energy barrier for both $*(O_L\text{–}O)$ formation and O_2 desorption steps in the LOM, thus facilitating the OER. This work provides a novel strategy to construct high-performance iron-based OER catalysts, presenting a promising solution for cost-effective industrial water splitting applications.

Author contributions

Q. H.: data curation, formal analysis, investigation, and writing – original draft. G. J. X.: methodology, data curation, formal analysis, and funding acquisition. B. H., D. X., and L. G.: formal analysis and analysis of supporting methodology. J. Wang, D. W., and L. G.: software and writing – original support draft. D. L., C. X., Z. W., and J. Wu: data curation and support visualization. F. X. and R. Z.: conceptualization. F. X., W. G. and R. Z.: funding acquisition, methodology, project administration, resources, supervision, and writing – review & editing. All the authors discussed the results and commented on the manuscript.

 This journal is © The Royal Society of Chemistry 2024

Open Access Article. Published on 14 kesäkuuta 2024. Downloaded on 13.5.2026 1.36.10.
This article is licensed under a Creative Commons Attribution-NonCommercial 3.0 Unported Licence.

Data availability

The data supporting this article have been included as part of the ESI.†

Conflicts of interest

There are no conflicts to declare.

Acknowledgements

This work was financially supported by the National Natural Science Foundation of China (No. 52203361, 22203041), the Basic and Applied Basic Research Foundation of Guangdong Province (No. 2023A1515012351, 2021A1515110406) and the Sichuan Department of Science and Technology Program of China (No. 2022YFG0299). We thank Materials Processing and Analysis Center, Peking University for assistance with TEM characterization. The XPS measurements and analyses were supported by Shimadzu Analytical Applications Center. The computational resources were supported from the Dongguan Key Laboratory of Artificial Intelligence Design for Advanced Materials, China.

Notes and references

1 Z. Y. Yu, Y. Duan, X. Y. Feng, X. Yu, M. R. Gao and S. H. Yu, *Adv. Mater.*, 2021, **33**, 2007100.
2 Y. Zhao, D. P. Adiyeri Saseendran, C. Huang, C. A. Triana, W. R. Marks, H. Chen, H. Zhao and G. R. Patzke, *Chem. Rev.*, 2023, **123**, 6257–6358.
3 S. Zhang, C. Tan, R. Yan, X. Zou, F. L. Hu, Y. Mi, C. Yan and S. Zhao, *Angew. Chem., Int. Ed.*, 2023, **62**, e202302795.
4 M. Vanags, G. Kulikovskis, J. Kostjukovs, L. Jekabsons, A. Sarakovskis, K. Smits, L. Bikse and A. Šutka, *Energy Environ. Sci.*, 2022, **15**, 2021–2028.
5 L. Chong, G. Gao, J. Wen, H. Li, H. Xu, Z. Green, J. D. Sugar, A. J. Kropf, W. Xu and X.-M. Lin, *Science*, 2023, **380**, 609.
6 X. Kang, F. Yang, Z. Zhang, H. Liu, S. Ge, S. Hu, S. Li, Y. Luo, Q. Yu, Z. Liu, Q. Wang, W. Ren, C. Sun, H.-M. Cheng and B. Liu, *Nat. Commun.*, 2023, **14**, 3607.
7 Y. Ma, G.-M. Mu, Y.-J. Miao, D.-M. Lin, C.-G. Xu, F.-Y. Xie and W. Zeng, *Rare Met.*, 2022, **41**, 844–850.
8 W. Cao, X.-H. Gao, J. Wu, A.-Q. Huang, H. Hu and Z.-W. Chen, *ACS Catal.*, 2024, **14**, 3640–3646.
9 N. Zhang and Y. Chai, *Energy Environ. Sci.*, 2021, **14**, 4647.
10 J. Wang, Y. Gao, H. Kong, J. Kim, S. Choi, F. Ciucci, Y. Hao, S. Yang, Z. Shao and J. Lim, *Chem. Soc. Rev.*, 2020, **49**, 9154–9196.
11 Y. Wang, R. Yang, Y. Ding, B. Zhang, H. Li, B. Bai, M. Li, Y. Cui, J. Xiao and Z.-S. Wu, *Nat. Commun.*, 2023, **14**, 1412.
12 A. Grimaud, O. Diaz-Morales, B. Han, W. T. Hong, Y.-L. Lee, L. Giordano, K. A. Stoerzinger, M. T. M. Koper and Y. Shao-Horn, *Nat. Chem.*, 2017, **9**, 457–465.
13 J. Jin, J. Yin, Y. Hu, Y. Zheng, H. Liu, X. Wang, P. Xi and C. H. Yan, *Angew. Chem., Int. Ed.*, 2024, **63**, e202313185.
14 K. Xiao, Y. Wang, P. Wu, L. Hou and Z. Q. Liu, *Angew. Chem., Int. Ed.*, 2023, **135**, e202301408.
15 Y. Wu, Y. Zhao, P. Zhai, C. Wang, J. Gao, L. Sun and J. Hou, *Adv. Mater.*, 2022, **34**, 2202523.
16 Q. Zhang, W. Xiao, H. C. Fu, X. L. Li, J. L. Lei, H. Q. Luo and N. B. Li, *ACS Catal.*, 2023, **13**, 14975–14986.
17 X. Wang, H. Zhong, S. Xi, W. S. V. Lee and J. Xue, *Adv. Mater.*, 2022, **34**, 2107956.
18 Y. H. Wang, L. Li, J. Shi, M. Y. Xie, J. Nie, G. F. Huang, B. Li, W. Hu, A. Pan and W. Q. Huang, *Adv. Sci.*, 2023, **10**, 2303321.
19 Y. Ou, L. P. Twight, B. Samanta, L. Liu, S. Biswas, J. L. Fehrs, N. A. Sagui, J. Villalobos, J. Morales-Santelices, D. Antipin, M. Risch, M. C. Toroker and S. W. Boettcher, *Nat. Commun.*, 2023, **14**, 7688.
20 P. Ye, K. Fang, H. Wang, Y. Wang, H. Huang, C. Mo, J. Ning and Y. Hu, *Nat. Commun.*, 2024, **15**, 1012.
21 S. Xin, Y. Tang, B. Jia, Z. Zhang, C. Li, R. Bao, C. Li, J. Yi, J. Wang and T. Ma, *Adv. Funct. Mater.*, 2023, **33**, 2305243.
22 H. Y. Chen, L. Yang, R. X. Wang, W. J. Zhang, R. Liu, Y. Z. Yun, N. Wang, S. Ramakrishna, L. Jiao and Y. Z. Long, *Small*, 2023, **19**, 2304086.
23 P. Kuang, Z. Ni, B. Zhu, Y. Lin and J. Yu, *Adv. Mater.*, 2023, **35**, 2303030.
24 X. Yang, C. Xing, B. Zhang, X. Liu, H. Liang, G. Luo, G. Zhang, Z. Li, S. Zhao, J. Zhang, G. Wang and Y. Qin, *ACS Catal.*, 2022, **12**, 10849–10856.
25 Y. Guo, J. Li, G. Yuan, J. Guo, Y. Zheng, Y. Huang, Q. Zhang, J. Li, J. Shen, C. Shu, J. Xu, Y. Tang, W. Lei and H. Shao, *ACS Nano*, 2023, **17**, 18253–18265.
26 G. Mu, G. Wang, Q. Huang, Y. Miao, D. Wen, D. Lin, C. Xu, Y. Wan, F. Xie, W. Guo and R. Zou, *Adv. Funct. Mater.*, 2023, **33**, 2211260.
27 Y. Ma, Y. Miao, G. Mu, D. Lin, C. Xu, W. Zeng and F. Xie, *Nanomaterials*, 2021, **11**, 1847.
28 D. Tyndall, M. J. Craig, L. Gannon, C. McGuinness, N. McEvoy, A. Roy, M. García-Melchor, M. P. Browne and V. Nicolosi, *J. Mater. Chem. A*, 2023, **11**, 4067–4077.
29 C. Li, Y. Nakagawa, M. Tamura, A. Nakayama and K. Tomishige, *ACS Catal.*, 2020, **10**, 14624–14639.
30 S. Liu, W. Xue, Y. Ji, W. Xu, W. Chen, L. Jia, T. Zhu, Z. Zhong, G. Xu, D. Mei and F. Su, *Appl. Catal., B*, 2023, **323**, 122151.
31 B. Elsener, D. Atzei, A. Krolikowski, V. Rossi Albertini, C. Sadun, R. Caminiti and A. Rossi, *Chem. Mater.*, 2004, **16**, 4216–4225.
32 T. Liu, L. Zhao, D. Wang, J. Zhu, B. Wang and C. Guo, *RSC Adv.*, 2013, **3**, 25648–25651.
33 A. Medvedeva, E. Makhonina, L. Pechen, Y. Politov, A. Rumyantsev, Y. Koshtyal, A. Goloveshkin, K. Maslakov and I. Eremenko, *Materials*, 2022, **15**, 8225.
34 W. Li, J. Lv, D. Liu, W. Cai, X. Chen, Q. Huang, L. Wang and B. Wang, *Chem. Mater.*, 2023, **35**, 3892–3901.
35 N. Zhang, J. Wang, Q. Li, Y. Xin, L. Zheng, Y. Wang and Z. Zhang, *Chem. Eng. J.*, 2021, **426**, 131845.
36 X. Zhao, F. Wang, X. Kong, R. Fang and Y. Li, *Nat. Commun.*, 2022, **13**, 2591.

Open Access Article. Published on 14 kesäkuuta 2024. Downloaded on 13.5.2026 1.36.10.
This article is licensed under a Creative Commons Attribution-NonCommercial 3.0 Unported Licence.

37 Z.-J. Chen, J. Dong, J. Wu, Q. Shao, N. Luo, M. Xu, Y. Sun, Y. Tang, J. Peng and H.-M. Cheng, *Nat. Commun.*, 2023, **14**, 4210.
38 M. Li, X. Wang, K. Liu, H. Sun, D. Sun, K. Huang, Y. Tang, W. Xing, H. Li and G. Fu, *Adv. Mater.*, 2023, **35**, 2302462.
39 Z. He, J. Zhang, Z. Gong, H. Lei, D. Zhou, N. Zhang, W. Mai, S. Zhao and Y. Chen, *Nat. Commun.*, 2022, **13**, 2191.
40 Y. Qin, Y. Liu, Y. Zhang, Y. Gu, Y. Lian, Y. Su, J. Hu, X. Zhao, Y. Peng, K. Feng, J. Zhong, M. H. Rummeli and Z. Deng, *ACS Catal.*, 2023, **13**, 256–266.
41 X. Chen, Q. Wang, Y. Cheng, H. Xing, J. Li, X. Zhu, L. Ma, Y. Li and D. Liu, *Adv. Funct. Mater.*, 2022, 2112674.
42 Y. Zhai, X. Ren, Y. Sun, D. Li, B. Wang and S. Liu, *Appl. Catal., B*, 2023, **323**, 122091.
43 C. Lin, J.-L. Li, X. Li, S. Yang, W. Luo, Y. Zhang, S.-H. Kim, D.-H. Kim, S. S. Shinde, Y.-F. Li, Z.-P. Liu, Z. Jiang and J.-H. Lee, *Nat. Catal.*, 2021, **4**, 1012–1023.
44 Y. Wen, P. Chen, L. Wang, S. Li, Z. Wang, J. Abed, X. Mao, Y. Min, C. T. Dinh, P. D. Luna, R. Huang, L. Zhang, L. Wang, L. Wang, R. J. Nielsen, H. Li, T. Zhuang, C. Ke, O. Voznyy, Y. Hu, Y. Li, W. A. Goddard Iii, B. Zhang, H. Peng and E. H. Sargent, *J. Am. Chem. Soc.*, 2021, **143**, 6482–6490.
45 F. Q. Wang, P. C. Zou, Y. Y. Zhang, W. L. Pan, Y. Li, L. M. Liang, C. Chen, H. Liu and S. J. Zheng, *Nat. Commun.*, 2023, **14**, 6019.
46 C. Rong, S. Wang, S. Xin, C. Jia, Q. Sun, Q. Zhang and C. Zhao, *Energy Environ. Sci.*, 2024, **17**, 4196–4204.
47 T. W. van Deelen, C. Hernández Mejía and K. P. de Jong, *Nat. Catal.*, 2019, **2**, 955–970.
48 G.-J. Xia, Y. Fu, W. Cao, J. Li and Y.-G. Wang, *Nano Res.*, 2024, DOI: **10.1007/s12274-024-6625-2**.
49 B. Qiu, C. Wang, N. Zhang, L. Cai, Y. Xiong and Y. Chai, *ACS Catal.*, 2019, **9**, 6484–6490.
50 Y. Yang, M. Lin, Y. Song, G. Tuerhong, J. Dai, T. Zhang, D. Guo and L. Liu, *J. Alloys Compd.*, 2022, **910**, 164869.

 This journal is © The Royal Society of Chemistry 2024